Chapter 7
^{19}F MRI Probes with Tunable Chemical Switches

Kazuya Kikuchi and Tatsuya Nakamura

7.1 Magnetic Resonance Imaging

MRI is the imaging technique based on nuclear magnetic resonance (NMR) phenomena. MRI offers high resolution, deep tissue imaging, and no radiation exposure (Louie et al. 2000). To acquire high contrast images, contrast agents such as Gd^{3+} complexes and superparamagnetic iron oxide nanoparticle (SPIO) are widely used in the field of clinical and research (Fig. 7.1) (Lee et al. 2008). Gd^{3+} complexes shorten the longitudinal relaxation time (T_1), results in enhancement of MRI signals. SPIO shorten the tranverse relaxation time (T_2), results in attenuation of MRI signal intensities. Figure 7.2 shows the switching OFF/ON type probes based on Gd^{3+} complexes and SPIO (Perez et al. 2002). However, ^{1}H MRI often suffers from high background signals derived from water and lipid etc. Therefore, there is a limitation of monitoring of biological signals.

Recently, heteronuclear MRI has been attracted considerable attentions as the alternative ^{1}H MRI. Several non proton MRI such as ^{13}C, ^{15}N, ^{19}F, ^{29}Si, ^{31}P, and ^{129}Xe has been utilized in biological analysis (Table 7.1) (Cassidy et al. 2013). Among these non proton MRI, ^{19}F MRI has considerable attentions, because fluorine has a 100% natural abundance and a high gyromagnetic ratio (Ahrens et al. 2005). In our bodies, there are a large amount of fluorine atoms in bones and teeth and almost no fluorine atoms in tissues. However, these fluorine atoms are immobilized in a solid state, exhibits very short T_2 which results in invisible MRI. Therefore, the ^{19}F MRI can acquire the image without the background signals.

Electronic Supplementary Material The online version of this chapter (https://doi.org/10.1007/978-981-13-7908-6_7) contains supplementary material, which is available to authorized users.

K. Kikuchi (✉) · T. Nakamura
Graduate School of Engineering, Osaka University, Suita City, Osaka, Japan
e-mail: kkikuchi@mls.eng.osaka-u.ac.jp

Y. Toyama et al. (eds.), *Make Life Visible*,
https://doi.org/10.1007/978-981-13-7908-6_7

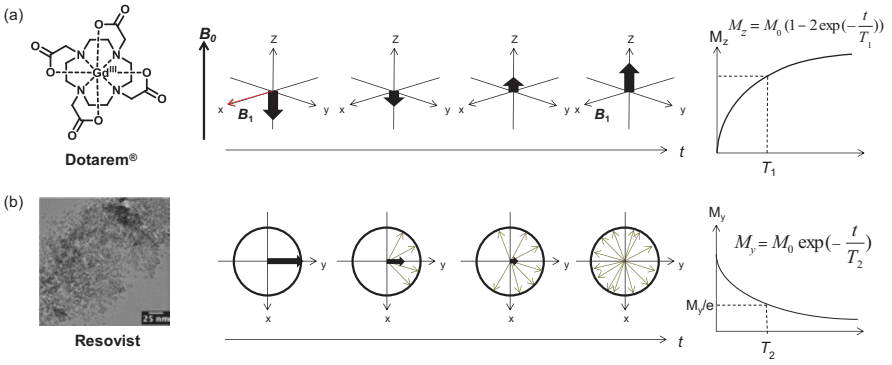

Fig. 7.1 (**a**) Clinically utilized T_1 contrast agent, Dotarem®, and T_1 relaxation. (**b**) Clinically utilized T_2 contrast agent, Resovist, and T_2 relaxation

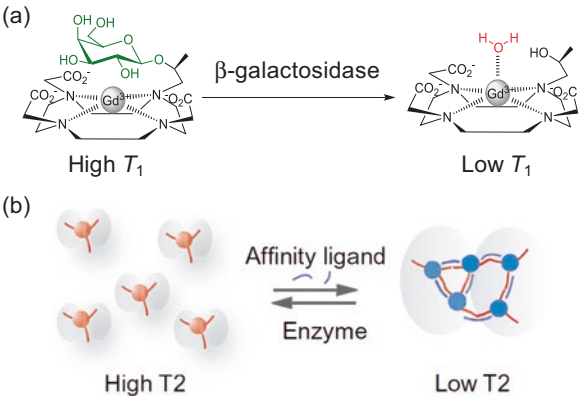

Fig. 7.2 The switching OFF/ON type probes based on (**a**) Gd^{3+} complexes and (**b**) SPIO

Table 7.1 NMR observable nucleus and the sensitivity

Nuclei	Resonant frequency (MHz·T^{-1})	Relative sensitivity	Natural abundance (%)	NMR sensitivity
^{1}H	42.58	1	99.985	1
^{13}C	10.71	1.59×10^{-2}	1.108	1.76×10^{-4}
^{15}N	4.31	1.04×10^{-3}	0.37	3.85×10^{-6}
^{19}F	40.05	8.33×10^{-1}	100	8.33×10^{-1}
^{29}Si	8.46	7.84×10^{-3}	4.70	3.69×10^{-4}
^{31}P	17.24	6.63×10^{-2}	100	6.63×10^{-2}
^{129}Xe	11.78	2.12×10^{-2}	26.4	5.60×10^{-3}

Toward this ends, ^{19}F MRI contrast agents (always ON type probes) have been utilized in visualization of foci, and cell tracker (Ahrens et al. 2005; Thurecht et al. 2010; Srinivas et al. 2007). In particular, perfluorocarbon (PFC) encapsulated nanoemulsions have attracted significant attention as highly sensitive ^{19}F MRI contrast

agents (Srinivas et al. 2010), and have been utilized as a cell tracker, and oxygen delivery. Recently, several activatable ^{19}F MRI probes (switching OFF/ON type probes) have also been developed. However, there are only a few examples of in vivo applications owing to the low sensitivity of such probes.

7.2 Perfluorocarbon Encapsulated in Silica Nanoparticle (FLAME)

In the author's research group, novel unique shape nanomaterials, which are perfluoro-15-crown-5 ether (PFCE)-encapsulated silica nanoparticles, FLAMEs (**FL**uorine **A**ccumulated silica nanoparticle for **M**RI contrast **E**nhancement), were developed (Fig. 7.3) (Matsushita et al. 2014). FLAMEs are composed of a liquid PFCE, which shows the high molecular mobility to achieve the long T_2, and a silica shell, which can be easily surface-modified for various functionalization. Although Ahrens et al. reported lipid-based PFCE nanoemulsions as ^{19}F MRI contrast agents for immune cell tracking (Ahrens et al. 2005; Srinivas et al. 2007), the chemical modification of the lipid emulsion surface is limited due to the unstablity in organic solvents. In contrast, the silica shell fulfills the many demands such as high hydrophilicity, high stability in both aqueous and organic solutions, and chemically surface-modifiable property. In fact, various surface functionalization of FLAMEs was achieved and the functionalized FLAMEs were useful for monitoring a reporter protein expression in living cells and in vivo detection of a tumor. These biological applications represent only a fraction of the forthcoming applications.

7.3 Paramagnetic Relaxation Enhancement (PRE) Effect

There are three types of paramagnetic effects: paramagnetic relaxation enhancement (PRE) effect, pseudocontact shifts (PCSs), and residual dipolar couplings (RDCs) (Clore and Iwahara 2009). Since PCSs and RDCs are observed only in anisotropic electron systems, only PRE is effective in the case of SPIO and Gd^{3+}

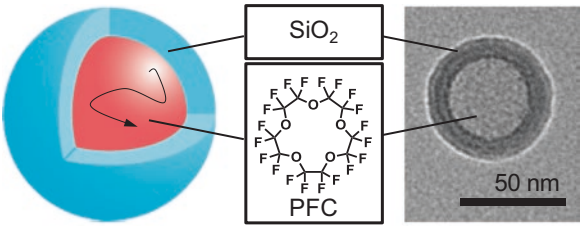

Fig. 7.3 Illustration and transmission electron microscope image of FLAME. The molecular motion of PFC is highly retained and thus the sensitivity of the nanoparticles is high sensitive

complexes (Keizer et al. 2007). The PRE decreases the spin-spin relaxation time (T_2) and results in the broadening of the NMR signals and the decrease of the MRI signals. There are two types of the relaxation mechanism of PRE effect. One is PRE through dipole-dipole interaction and the other is PRE through Curie-spin relaxation. The PRE effect of Gd^{3+} complexes is occurred through dipole-dipole interaction. The transverse (Γ_2) PRE rates of Gd^{3+} are described by the Solomon–Bloembergen (SB) equations (Solomon 1955; Bloembergen and Morgan 1961; Lipari and Szabo 1982):

$$\Gamma_2 = \frac{1}{15}\left(\frac{\mu_0}{4\pi}\right)^2 \gamma_I^2 g^2 \mu_B^2 S(S+1)\left\{4J_{SB}(0) + 3J_{SB}(\omega_I)\right\}$$

where μ_0 is the permeability of free space, μ_B is the magnetic moment of the free electron, γ_I the fluorine gyromagnetic ratio, g is the electron g-factor, S is the electron spin quantum number, and $\omega_I/2\pi$ is the Larmor frequency of the fluorine compound. $J_{SB}(\omega)$ is the spectral density function;

$$J_{SB}(\omega) = r^{-6}\frac{\tau_C}{1+(\omega\tau_C)^2}$$

τ_C is the correlation time, defined as $(\tau_r^{-1} + \tau_s^{-1})^{-1}$. τ_r is the rotational correlation time of the molecule, and τ_s is the effective electron relaxation time.

In contrast, Curie-spin relaxation arises from dipole-dipole interaction between a observable nuclide and the magnetization of the electron. The PRE effect of SPIOs is governed by Curie-spin relaxations owing to their high magnetic susceptibility. The Γ_2 PRE rates of Curie-spin relaxation are given by (Bertinin et al. 2002):

$$\Gamma_2 = \frac{1}{5}\left(\frac{\mu_0}{4\pi}\right)^2 \frac{\omega_I g^4 \mu_B^4 S^2 (S+1)^2}{(3k_B T)^2 r^6}\left(4\tau_r + \frac{3\tau_r}{1+\omega_I^2 \tau_r^2}\right)$$

where k_B is the Boltzmann constant, T is temperature.

In both cases, PRE effect is effective over short distance due to its r^{-6} dependency, where r is the distance between NMR-observable nuclei and a paramagnetic center. When the T_2 relaxivity of SPIO is compared with that of Gd^{3+} complexes, SPIOs have higher T_2 relaxivity than Gd^{3+} complexes (Table 7.2). Thus, SPIO is efficient for decreasing the ^{19}F NMR/MRI signals of PFCE near the FLAME core compared with Gd^{3+} complexes.

Table 7.2 Relaxivities (mM^{-1} s^{-1}) of paramagnetic contrast agents in H_2O at 37 °C (Rohrer et al. 2005)

	0.47 T			1.5 T			3.0 T			4.7 T		
	r_1	r_2	r_2/r_1	r_1	r_2	r_2/r_1	r_1	r_2	r_2/r_1	r_1	r_2	r_2/r_1
Gd^{3+} complex												
Magnevist	3.4	4.0	1.18	3.3	3.9	1.18	3.1	3.7	1.19	3.2	4.0	1.25
Gadovist	3.7	5.1	1.38	3.3	3.9	1.18	3.2	3.9	1.22	3.2	3.9	1.22
ProHance	3.1	3.7	1.19	2.9	3.2	1.10	2.8	3.4	1.21	2.8	3.7	1.32
MultiHance	4.2	4.8	1.14	4.0	4.3	1.08	4.0	4.7	1.18	4.0	5.0	1.25
Dotarem	3.4	4.1	1.21	2.9	3.2	1.10	2.8	3.3	1.18	2.8	3.7	1.32
OmniScan	3.5	3.8	1.09	3.3	3.6	1.09	3.2	3.8	1.19	3.3	4.1	1.24
Teslascan	1.9	2.1	1.11	1.6	2.1	1.31	1.5	2.3	1.53	1.6	2.7	1.69
Optimark	4.2	5.2	1.24	3.8	4.2	1.11	3.6	4.5	1.25	3.8	4.7	1.24
SPIO												
Resovist	20.6	86	4.17	8.7	61	7.01	4.6	143	31.1	2.8	176	62.9
Feridex	27	152	5.63	4.7	41	8.72	4.1	93	22.7	2.3	105	45.7

7.4 Gadolinium Based-^{19}F MRI Nanoprobe for Monitoring Reducing Environment

PRE effect is effective over short distance due to its r^{-6} dependency, where r is the distance between NMR-observable nuclei and a paramagnetic center (Clore and Iwahara 2009; Iwahara and Clore 2006). The author's research group has employed PRE effect to develop activatable ^{19}F MRI small molecule probes for detection of enzyme activity (Mizukami et al. 2008). The probes consist of fluorine compound, enzyme substrate, and Gd^{3+} complex. Gd^{3+} complex was conjugated with fluorine compounds through enzyme substrate. The distance between fluorine compound and Gd^{3+} complex was approximately 2.2 nm, determined by molecular mechanic method. Since PRE effect is effective at such close distance, ^{19}F NMR/MRI signal of the probes were decreased. Upon addition of enzyme, Gd^{3+} complexes were away from fluorine compounds, which results in high ^{19}F NMR/MRI signal enhancements.

In the case of FLAME, most of PFCE compounds are more than 50 Å away from the surface-modified Gd^{3+} complexes due to the thickness of the silica shell. Thus, it was assumed that the PRE effect might not sufficiently attenuate the ^{19}F NMR/MRI signals of FLAME.

The authors first confirmed whether the PRE of the Gd^{3+} complexes on the FLAME surface was effective. Different concentration of Gd^{3+} diethylenetriamine-pentaacetate (DTPA) complexes were attached to FLAME to yield FLAME-

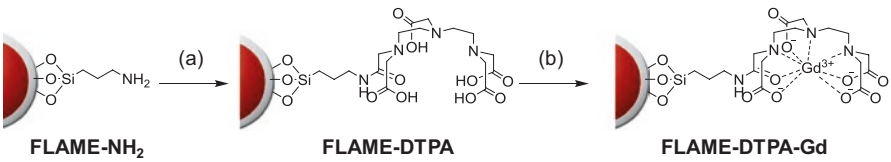

Scheme 7.1 Preparation of FLAME-DTPA-Gd. (**a**) diethylenetriaminepentaacetic acid dianhydride, TEA, DMF; (**b**) $GdCl_3 \cdot 6H_2O$, methanol

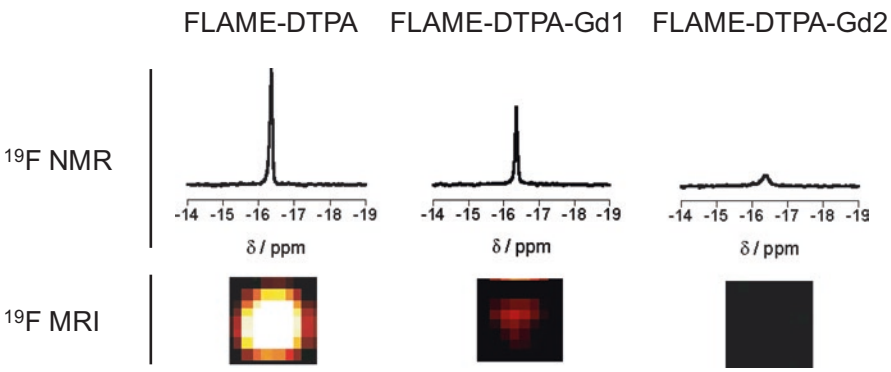

Fig. 7.4 ^{19}F NMR spectra and ^{19}F MRI phantom images of FLAME-DTPA and FLAME-DTPA-Gd. For ^{19}F NMR, $C_{PFCE} = 0.6$ mM, and the accumulation time was 1 min 22 s. For ^{19}F MRI (Rapid Acquisition with the Refocused Echoes (RARE) method): T_R was 3000 ms. $T_{E,eff}$ was 12 ms. The NEX was 64. The acquisition time was 12 min 48 s

DTPA-Gd1–2 (Scheme 7.1). The ^{19}F NMR spectrum of FLAME-DTPA without Gd^{3+} exhibited a sharp, single peak (T_2 = 420 ms). Meanwhile, that of FLAME-DTPA-Gd became a broader peak as Gd^{3+} concentration increased (Fig. 7.4a). The T_2 of FLAME-DTPA-Gds decreased in Gd^{3+} concentration dependent manner (T_2 = 68, 40 ms for FLAME-DTPA-Gd1, 2 respectively). Although the ^{19}F MRI signal of FLAME-DTPA were observed due to the long T_2, that of FLAME-DTPA-Gd was decreased with Gd^{3+} concentration increasing (Fig. 7.4b). These results indicated that the ^{19}F NMR/MRI signals of PFCE in FLAME were affected by the PRE from the surface-modified Gd^{3+} complexes. Therefore, the author expected that activatable ^{19}F MRI probes with high ^{19}F MRI signal enhancement would be achieved by introducing a cleavable linker between FLAME and the surface-modified Gd^{3+} complexes.

This result was explained by the molecular mobility on the NMR/MRI measurement time scale. Iwahara et al. reported that the PRE effect was efficient in spite of the long average distance, when NMR-observable nuclei can occasionally enter the effective range of the PRE effect (Lee et al. 2008). The long T_2 indicates that the PFCE in FLAME maintains high molecular mobility even in the nanoparticle structure (Matsushita et al. 2014). Although the PFCE at the center of the FLAME core is about 250 Å away from the surface Gd^{3+} complexes (where PRE is not efficient),

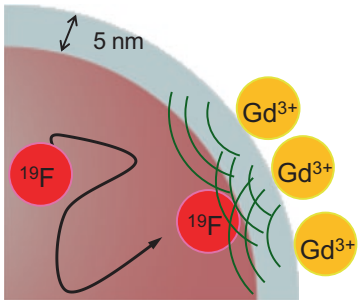

Fig. 7.5 Proposed relaxation mechanism of fluorine compounds in FLAME

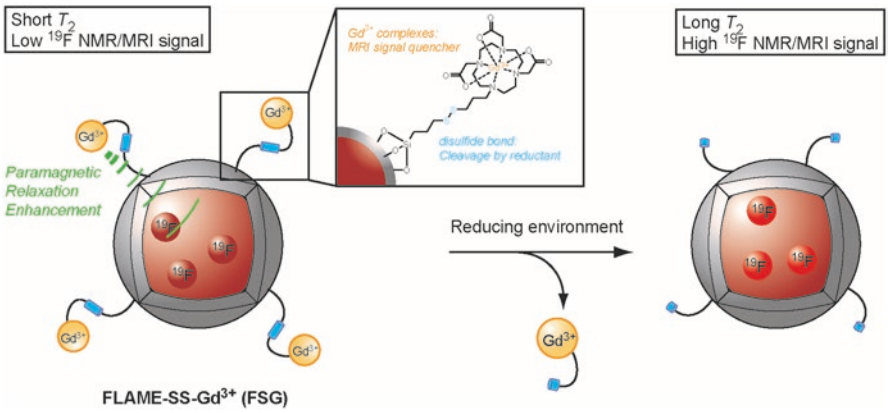

Fig. 7.6 Design of activatable FLAME, FLAME-SS-Gd^{3+} (FSG)

the fluorine compounds can access the inner shell of FLAME on the measurement time scale. Near the inner shell, although the contribution of one Gd^{3+} complex to the PRE effect is small, the PRE effect from multiple surface Gd^{3+} complexes is combined, and thus the T_2 of PFCE is efficiently decreased (Fig. 7.5). Although Grüll et al. observed the PRE of PFCE in Gd^{3+}-modified nanoemulsions, where the distance between the Gd^{3+} complexes and the fluorine core was less than 22 Å (De Vries et al. 2014), we confirmed that the PRE was effective as such distance for the first time.

Next, the authors designed activatable FLAMEs, FLAME-SS-Gd^{3+} (FSG), to image reducing environments. Gd^{3+} complexes were attached to the FLAME surface via disulfide linkers to reduce the T_2 of the fluorine compounds by the PRE effect, which attenuates the ^{19}F NMR/MRI signals (Fig. 7.6). When the disulfide of FSG was reduced, the Gd^{3+} complexes were cleaved from the FLAME surface. Then, the T_2 of the encapsulated PFCE would be elongated and the ^{19}F NMR/MRI signal intensity would increase.

To optimize the amount of Gd^{3+} complexes on the surface of FLAMEs, three types of FSGs with different concentrations of Gd^{3+} were prepared (Scheme 7.2). The synthetic intermediate FLAME-Py was prepared by the reaction of FLAME

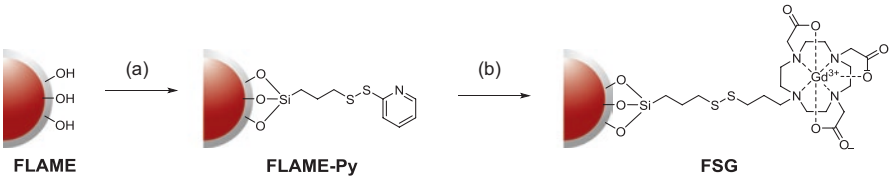

Scheme 7.2 Preparation of FLAME-SS-Gd^{3+} (FSG). (**a**) 2-((3-(trimethoxysilyl)propyl) dithio) pyridine, isopropanol; (**b**) Gd-DOTA-SH, MeOH

Table 7.3 Physical properties of FLAME and FSGs

	ς-potential/mV	$\boldsymbol{n}_{19F}$[a]	$\boldsymbol{n}_{Gd}$[a]	$\boldsymbol{n}_{19F}/\boldsymbol{n}_{Gd}$[a]	$T_{2,\,TCEP-}$/ms	$T_{2,\,TCEP+}$/ms
FLAME	−24.8 ± 1.7	1.7×10^6	0	–	420	–[b]
FSG1	−12.6 ± 2.4	1.7×10^6	9.1×10^2	1.8×10^3	120	383
FSG2	3.9 ± 1.4	1.7×10^6	2.1×10^3	7.7×10^2	66	365
FSG3	5.7 ± 1.5	1.7×10^6	3.1×10^3	5.3×10^2	27	371

$\boldsymbol{n}_{19F}$: the number of ^{19}F atoms in one nanoparticle, $\boldsymbol{n}_{Gd}$ the number of Gd^{3+} atoms in one nanoparticle

[a]These values were predicted assuming that FSG has a single size of 53.4 nm (diameter)

[b]Not measured

with different amounts of 2-((3-(trimethoxysilyl)propyl)dithio)pyridine (1 eq. for FSG1, 10 eq. for FSG2, and 100 eq. for FSG3). Then, 1 eq., 10 eq., or 100 eq. of Gd^{3+} complexes were conjugated to the FLAMEs via a thiol-disulfide exchange reaction to afford FSG1–3, respectively.

Next, the number of fluorine atoms and Gd^{3+} ions per nanoparticle were calculated as $\boldsymbol{n}_{19F}$ and $\boldsymbol{n}_{Gd}$, respectively (Table 7.3). The quantity of attached Gd^{3+} ions was measured by inductively coupled plasma atomic emission spectrometry (ICP-AES), and the amount of the fluorine atoms was quantified by ^{19}F NMR in comparison with that of an internal standard, sodium trifluoroacetate. The average diameter of FLAME was 53.4 nm with a 5 nm-thick silica shell, as measured by transmission electron microscopy. If FLAME has a single size of 53.4 nm, the mole of PFCE per one nanoparticle (m_{PFCE}) could be calculated as follows:

$$m_{PFCE} = \frac{w_{PFCE}}{MW_{PFCE}} = \frac{d_{PFCE} \times V_{core}}{MW_{PFCE}} = \frac{d_{PFCE} \times \frac{4}{3}\pi r_{core}^3}{MW_{PFCE}} \approx 1.4 \times 10^{-19} \left(\text{mol / particle}\right)$$

where w_{PFCE} is the weight of PFCE in FLAME, MW_{PFCE} is the molecular weight of PFCE, d_{PFCE} is the density of PFCE (1.86 g/cm^3), V_{core} is the volume of PFCE in FLAME, and r_{core} is the radius of the FLAME core (21.7 nm). Thus, the number of fluorine atoms per one nanoparticle ($\boldsymbol{n}_{19F}$) was calculated as:

$$n_{^{19}F} = m_{PFCE} \times 20 \times N_A \approx 1.7 \times 10^6 \left(^{19}\text{F atom / particle}\right)$$

where N_A is Avogadro's constant. Since the amount of the Gd^{3+} ions was measured by ICP-AES, the molar ratio of the Gd^{3+} ions to PFCE for FSG1, FSG2, and FSG3 was calculated to be 0.011, 0.026, and 0.038, respectively. Therefore, the number of Gd^{3+} ions per nanoparticle ($\boldsymbol{n}_{Gd}$) was calculated as:

$$\mathrm{FSG1}: m_{Gd^{3+}} / m_{PFCE} = 0.011$$

$$n_{Gd} = m_{Gd^{3+}} \times N_A = 0.011 \times m_{PFCE} \times N_A \approx 9.1 \times 10^2 \left(\mathrm{particle}^{-1}\right)$$

$$\mathrm{FSG2}: m_{Gd^{3+}} / m_{PFCE} = 0.026$$

$$n_{Gd} = m_{Gd^{3+}} \times N_A = 0.026 \times m_{PFCE} \times N_A \approx 2.1 \times 10^3 \left(\mathrm{particle}^{-1}\right)$$

$$\mathrm{FSG3}: m_{Gd^{3+}} / m_{PFCE} = 0.038$$

$$n_{Gd} = m_{Gd^{3+}} \times N_A = 0.038 \times m_{PFCE} \times N_A \approx 3.1 \times 10^3 \left(\mathrm{particle}^{-1}\right)$$

The ς-potentials of FSGs gradually shifted towards the positive direction with increasing amounts of surface Gd^{3+} ions (Table 7.3). This was because the slightly electronegative silanol groups on the FLAME surface were decreased owing to the coupling with 2-((3-(trimethoxysilyl)propyl)dithio)pyridine. The $\boldsymbol{n}_{Gd}$ and ς-potential data indicated that different concentrations of Gd^{3+} complexes were successfully introduced on the FLAME surface.

The ^{19}F NMR spectrum of FLAME without paramagnetic ions exhibited a sharp peak. In contrast, the ^{19}F NMR peaks of FSGs were decreased and more broad according to the concentration of surface Gd^{3+} on account of the PRE effect (Fig. 7.7a). Although the ^{19}F NMR of FSG1 exhibited a sharp peak, the T_2 of FSG1 (120 ms) was shorter than that of FLAME (420 ms) (Table 7.3). The T_2 of FSG2 and FSG3 was 66 ms, 27 ms, respectively. As such, the PRE effect was observed in all FSGs.

^{19}F NMR spectra and T_2 of FSGs were measured after treatment with a reducing agent, tris(2-carboxyethyl)phosphine (TCEP) (Fig. 7.7). Addition of TCEP made the ^{19}F NMR peaks of all FSGs sharper and taller as compared to those before the addition. The T_2 values of FSG1–3 were significantly increased upon addition of TCEP within 2 h, and were comparable to that of FLAME. All Gd^{3+} complexes were cleaved upon addition of more than 2 mM TCEP (Fig. 7.7b). The highest ^{19}F NMR SNR of FSG1–3 was obtained at 2 mM TCEP, and the values were 16.2 for FSG1, 19.5 for FSG2, and 17.9 for FSG3. The signal enhancement factors in response to the reductant were 3.1, 9.7, and 12.7 for FSG1–3, respectively. Thus, FSG3 was the most sensitive ^{19}F NMR probe in the detection of the reducing environment.

The ^{19}F NMR signals of the FSGs increased upon addition of other reducing agents such as glutathione, cysteine, and dithiothreitol (Fig. 7.8). In particular, addition of glutathione induced the greatest ^{19}F NMR signal enhancement. Although there are some concerns about the stability of reduction-triggered nanoparticles in normal tissues, rational optimization of the disulfide linkage will lead to practical in vivo applications.

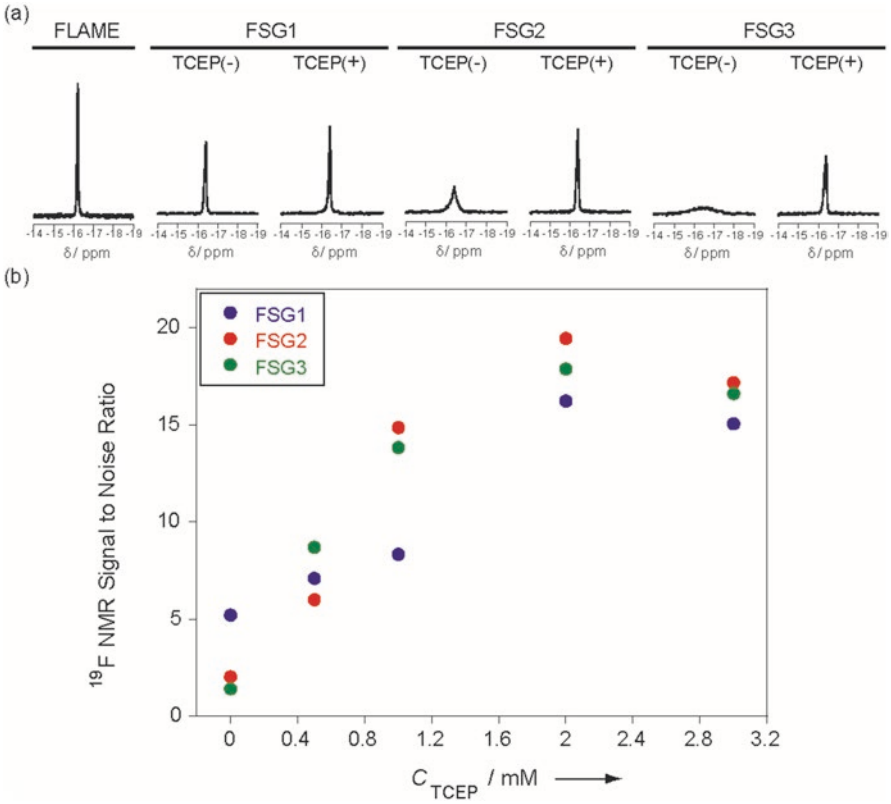

Fig. 7.7 (**a**) ^{19}F NMR spectra of FSGs incubated with or without TCEP. C_{PFCE}: 0.6 mM, C_{TCEP}: 1.0 mM, incubation time: 4 h, accumulation time: 10 min 55 s. (**b**) ^{19}F NMR signal to noise ratio of FSGs in the presence of TCEP (Blue: FSG1, Red: FSG2, Green: FSG3). C_{PFCE}: 0.15 mM

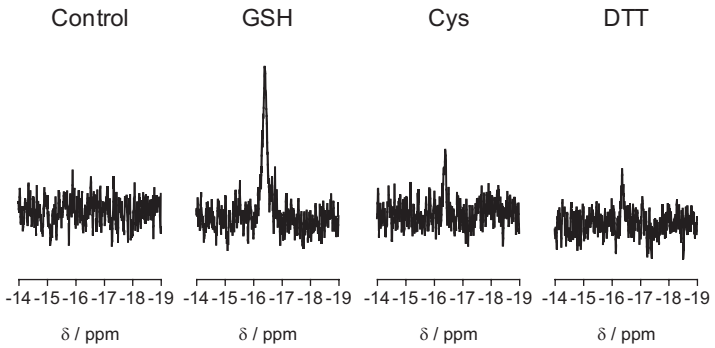

Fig. 7.8 ^{19}F NMR spectra of FSG2 (C_{PFCE} = 0.15 mM) incubated with several thiol-based reducing agents (3 mM). Left to right, control (without reductant), glutathione (GSH), cysteine (Cys), 1,4-dithiothreitol (DTT). The accumulation time was 1 min 22 s. Incubation time was 4 h

Finally, ^{19}F MR phantom images of FSGs solutions with or without TCEP were obtained by varying $T_{E,eff}$. In general, the MRI signal of the long T_2 component is well observed at both short and long $T_{E,eff}$. In contrast, the MRI signal of samples with moderately short T_2 is only visible at short $T_{E,eff}$, and that of the extremely short T_2 component is not observed even at short $T_{E,eff}$. As expected from the ^{19}F NMR results, almost no ^{19}F MRI signals of FSG2 and FSG3 were detected without TCEP at any $T_{E,eff}$ due to the strong PRE effect (Fig. 7.9a, b). In contrast, the ^{19}F MRI signals of FSG1 were observed at $T_{E,eff} \leq 84$ ms because of the moderately short T_2. However, the measurement of FSG1 without TCEP at $T_{E,eff} \geq 108$ ms extinguished the undesired ^{19}F MRI signals. Reductive reactions induced a noticeable ^{19}F MRI signal enhancement in FSG1–3 at any $T_{E,eff}$ (filled circles). At $T_{E,eff} = 12$ ms, approximately 60- and 40-fold increases were observed in FSG2 and FSG3, respectively. Although the signal the enhancement of FSG1 was only two-fold at $T_{E,eff} = 12$ ms, a 50-fold increase was observed at $T_{E,eff} = 108$ ms. These results indicated that FSG2 was the most effective probe for detecting reducing environments. One of the advantages of FSGs is the high sensitivity, because the ^{19}F NMR/MRI signals of 1.7×10^6 fluorine atoms in the core were decreased by ca. 1.0×10^3 Gd^{3+} complexes on the

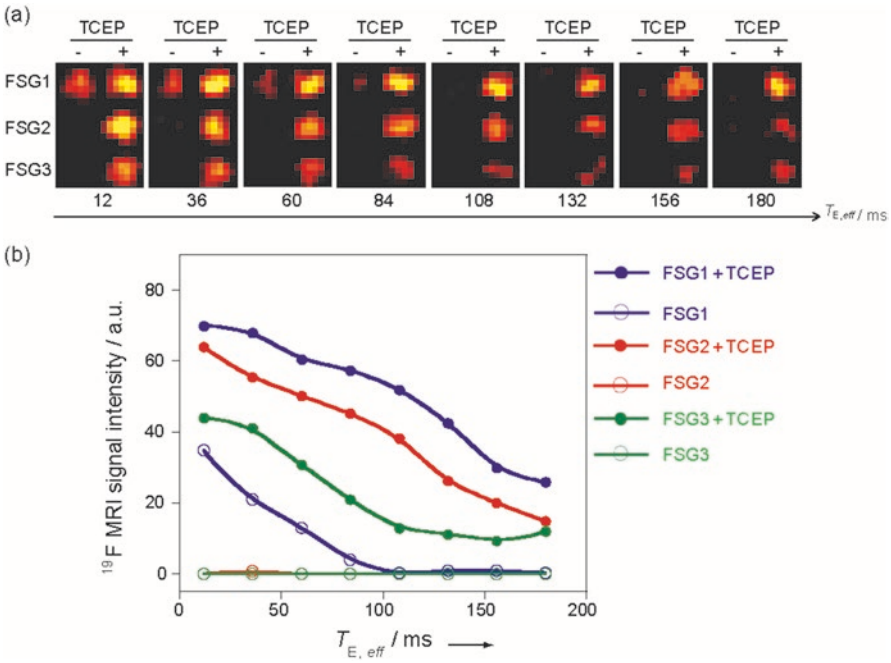

Fig. 7.9 ^{19}F MRI signal enhancement of FSGs by TCEP. (**a**) ^{19}F MRI phantom images of FSG1–3 with or without TCEP. (**b**) Plot of ^{19}F MRI signal intensity of FSG1–3 at different $T_{E,eff}$ with (filled circles) or without (open circles) TCEP. ^{19}F MRI RARE method: the matrix size was 128 × 64 and the slice thickness was 30 mm. T_R was 3000 ms. The NEX was 64. The acquisition time was 25 min 36 s

FLAME surface. The ratios of fluorine atoms to Gd^{3+} complexes (Table 7.1) are the highest among known PRE-based probes, of which the ratios were single digits. This high ratio led to the high signal amplification.

References

Ahrens ET, Flores R, Xu H, Morel PA (2005) In vivo imaging platform for tracking immunotherapeutic cells. Nat Biotechnol 23:983–987

Bertinin I, Luchinat C, Parigi G (2002) Magnetic susceptibility in paramagnetic NMR. Prog Nucl Mag Res Sp 40:249–273

Bloembergen N, Morgan LO (1961) Proton relaxation times in paramagnetic solutions. Effects of electron spin relaxation. J Chem Phys 34:842–850

Cassidy MC, Chan HR, Ross BD, Bhttacharya PK, Marcus CM (2013) In vivo magnetic resonance imaging of hyperpolarized silicon particles. Nat Nanotechnol 8:363–368

Clore GM, Iwahara J (2009) Theory, practice, and applications of paramagnetic relaxation enhancement for the characterization of transient low-population states of biological macromolecules and their complexes. Chem Rev 109:4108–4139

De Vries A, Moonen R, Yildirim M, Langereis S, Lamer-Ichs R, Pikkemaat JA, Baroni S, Terreno E, Nicolay K, Strijkers GJ, Grüll H (2014) Relaxometric studies of gadolinium-functionalized perfluorocarbon nanoparticles for MR imaging. Contrast Media Mol Imaging 9:83–91

Iwahara J, Clore GM (2006) Detecting transient intermediates in macromolecular binding by paramagnetic NMR. Nature 440:1227–1230

Keizer PHJ, Desreux JF, Overhand M, Ubbink M (2007) Increased paramagnetic effect of a lanthanide protein probe by two-point attachment. J Am Soc Chem 129:9292–9293

Lee H, Sun E, Ham D, Weissleder R (2008) Chip–NMR biosensor for detection and molecular analysis of cells. Nat Med 14:869–873

Lipari G, Szabo A (1982) Model-free approach to the interpretation of nuclear magnetic resonance relaxation in macromolecules. 1. Theory and range of validity. J Am Chem Soc 104:4546–4559

Louie AY, Hüber MM, Ahrens ET, Rothbächer U, Moats R, Jacobs RE, Fraser SE, Meade TJ (2000) In vivo visualization of gene expression using magnetic resonance imaging. Nat Biotechnol 18:321–325

Matsushita H, Mizukami S, Sugihara F, Nakanishi Y, Yoshioka Y, Kikuchi K (2014) Multifunctional core-shell silica nanoparticles for highly sensitive19F magnetic resonance imaging. Angew Chem Int Ed 53:1008–1011

Mizukami S, Takikawa R, Sugihara F, Hori Y, Tochio H, Wälchli M, Shirakawa M, Kikuchi K (2008) Paramagnetic relaxation-based 19F MRI probe to detect protease activity. J Am Chem Soc 130:794–795

Perez JM, Josephson L, O'Loughlin T, Högemann D, Weissleder R (2002) Magnetic relaxation switches capable of sensing molecular interactions. Nat Biotechnol 20:816–820

Rohrer M, Bauer H, Mintorovitch J, Requardt M, Weinmann H-J (2005) Comparison of magnetic properties of MRI contrast media solutions at different magnetic field strengths. Investig Radiol 40:715–724

Solomon I (1955) Relaxation processes in a system of two spins. Phys Rev 99:559–595

Srinivas M, Morel PA, Ernst LA, Laidlaw DH, Ahrens ET (2007) Fluorine-19 MRI for visualization and quantification of cell migration in a diabetes model. Mang Reson Med 58:725–734

Srinivas M, Cruz LJ, Bonetto F, Heerschap A, Figdor CG, de Vries IJM (2010) Customizable, multi-functional fluorocarbon nanoparticles for quantitative in vivo imaging using 19F MRI and optical imaging. Biomaterials 31:7070–7077

Thurecht KJ, Blakey I, Peng H, Squires O, Hsu S, Alexander C, Whittaker AK (2010) Functional hyperbranched polymers: toward targeted in Vivo19F magnetic resonance imaging using designed macromolecules. J Am Chem Soc 132:5336–5337